Electron kinetic entropy across quasi-perpendicular shocks

M. Lindberg[1], A. Vaivads[1], S. Raptis[1], P.-A. Lindqvist[1], B. L. Giles[2], D. J. Gershman[2]

[1]Space and Plasma Physics, School of Electrical Engineering and Computer Science, KTH Royal Institute of Technology, Stockholm, Sweden

[2]NASA Goddard Space Flight Center, Greenbelt, USA

Key Points:

- The change in electron kinetic entropy per particle is calculated for 22 shock crossings having wide range of shock conditions
- The entropy change displays a strong dependence on the electron beta parameter
- The entropy change corresponds to an adiabatic index $\gamma_e = 1.595 \pm 0.036$

Corresponding author: Martin Lindberg, mli6@kth.se

Abstract

We use Magnetospheric Multiscale (MMS) data to study electron kinetic entropy across Earth's quasi-perpendicular bow shock. We have selected 22 shock crossings covering a wide range of shock conditions. Measured distribution functions are calibrated and corrected for spacecraft potential, secondary electron contamination, lack of measurements at the lowest energies and electron density measurements based on the plasma frequency measurements. The change in electron kinetic entropy per particle is calculated for 22 shock crossings. 20 out of 22 crossings display an increase in the electron kinetic entropy per particle ranging between 0.1-1.4 k_{B} while two crossings display a slight decrease of -0.06 k_{B}. We observe that the change in electron kinetic entropy, ΔS_{e}, displays a strong dependence on the change in electron temperature, ΔT_{e}, and the upstream electron plasma beta, β_{e}. Shocks with high ΔT_{e} are found to have high ΔS_{e}. Shocks with low upstream electron plasma betas are associated to higher ΔS_{e} than shocks with large electron plasma beta. We show that the calculated entropy per particle is strictly less than the maximum state of entropy obtained using a Maxwellian distribution function. The resulting change in electron kinetic entropy per particle ΔS_{e}, density Δn_{e} and temperature ΔT_{e} is used to determine a value for the adiabatic index of electrons. We find that an adiabatic index of $\gamma_{\mathrm{e}} = 1.595 \pm 0.036$ describes the observations best.

1 Introduction

Collisionless shock waves are ubiquitous throughout our universe. However, many questions remain about the physical mechanism behind electron heating (Schwartz et al., 2011; See et al., 2013; Chen et al., 2018) and entropy generation (Parks et al., 2012) at collisionless shocks. In the absence of collisions, dissipation of the solar wind bulk flow energy must be sustained via other processes. The physics behind dissipative processes and entropy generation in collisionless plasmas is an ongoing research topic and numerous studies have been performed observationally, experimentally, theoretically and numerically (Liang et al., 2019, 2020; Cassak, 2016; Howes, 2018).

Entropy generation is linked to irreversible dissipation in closed thermodynamic systems (Anderson, 2004; Blundell & Blundell, 2010). However, whether entropy can be used as a measure of dissipation in open thermodynamic systems is currently under debate (Liang et al., 2020). Liang et al. (2019) describe the development of using local kinetic entropy density as a diagnostic to indicate dissipation in magnetic reconnection events

as seen in numerical simulations. Another study uses the Cluster spacecraft ion and electron data to measure the entropy development across Earth's quasi-perpendicular bow shock (Parks et al., 2012). Both magnetic reconnection events and bow shock crossings are not closed systems. However, the concept of entropy has been successfully used to study the irreversible processes within those systems. In the case of the bow shock, this can be an important tool to distinguish the relative contribution of irreversible heating and adiabatic heating during the plasma compression across the shock. There has been few experimental studies of such an entropy development, one of the reasons being that this requires very accurate distribution function calibrations. Therefore, with the launch of the Magnetospheric Multiscale spacecraft (MMS) and it's high resolution particle instrumentation, it is of high importance to address this topic.

In this study, we use data from the Magnetospheric Multiscale (MMS) mission to investigate the change in electron kinetic entropy across quasi-perpendicular shocks. We provide a theoretical calculation (Appendix A) of the change in *total* entropy per particle across a collisionless shock and show its dependence on the upstream Alfvénic Mach number, M_{A}, shock angle, θ_{Bn}, and *total* plasma beta, β. The calculation assumes a one fluid MHD approximation considering both ions and electrons. No analytical expression is known considering electrons alone and hence comparing to the one fluid-model is of interest. Of particular importance is to study how the amount of generated kinetic entropy relates to the shock parameters, such as Alfvénic Mach number M_{A}, plasma beta β_{e}, shock angle θ_{Bn} and change in density Δn_{e} and temperature ΔT_{e}. Earlier studies have shown that there are two critical Whistler Mach numbers, discussed in Krasnoselskikh et al. (2002) and Lalti et al. (2020). Whistler waves can scatter electrons via the cyclotron resonance (Amano et al., 2020) and could possibly contribute to entropy generation, thus it is of importance to understand if these two different critical Mach numbers affect the electron entropy development across the shock.

To calculate the kinetic entropy across Earth's collisionless bow shock, we use the formulation defined within kinetic theory where the *entropy density* is calculated directly from the distribution function f according to Liang et al. (2019),

$$s = -k_{\mathrm{B}} \int f \ln f \mathrm{d}^3\mathbf{v}. \tag{1}$$

We normalize eq. (1) with the number density $n = \int f \mathrm{d}^3\mathbf{v}$ such that we obtain the entropy per particle

$$S = \frac{s}{n} = -\frac{k_\mathrm{B} \int f \ln f d^3\mathbf{v}}{\int f \mathrm{d}^3\mathbf{v}}. \tag{2}$$

In the rest of the article when referring to "entropy" we mean S, i.e. entropy per particle that in our case only consider electrons.

2 Method

2.1 Data

We use data from 22 shock crossings observed by the MMS spacecraft. All the selected events are during time periods when the burst data are available. The shock crossings are chosen such as to have a wide range of different shock conditions. Some of the crossings have been selected from the databases used in Raptis et al. (2020) and Lalti et al. (2020). Magnetic field data are taken from the fluxgate magnetometer (FGM), the measurement cadence is 7.8 ms. All plasma moments and the measured 3D distribution functions are obtained from the fast plasma investigation (FPI) measuring at a cadence 30 ms. Additional calibration of electron distribution functions is necessary as described later. The electric field spectra and spacecraft potential are obtained from the spin plane double probe (SDP) and the axial double probe (ADP) instruments. The solar wind ion-temperature is not resolved properly by MMS, therefore ion-temperature data is taken from the 1-min resolution OMNI database (King & Papitashvili, 2005).

2.2 Shock parameter calculations

2.2.1 Shock Normal

The shock normal direction is determined using upstream and downstream measurements of the magnetic field and ion velocity at MMS1. The normal vector is calculated and compared using five different methods:

The *magnetic coplanarity method*, using only magnetic field data,

$$\hat{\mathbf{n}}_\mathrm{MC} = \pm \frac{(\mathbf{B}_\mathrm{d} \times \mathbf{B}_\mathrm{u}) \times \Delta\mathbf{B}}{|(\mathbf{B}_\mathrm{d} \times \mathbf{B}_\mathrm{u}) \times \Delta\mathbf{B}|} \tag{3}$$

The *velocity coplanarity method*, using only ion velocity data,

$$\hat{\mathbf{n}}_\mathrm{VC} = \pm \frac{\mathbf{V}_\mathrm{d} - \mathbf{V}_\mathrm{u}}{|\mathbf{V}_\mathrm{d} - \mathbf{V}_\mathrm{u}|} \tag{4}$$

and three *mixed methods* using both magnetic field and ion velocity data,

$$\hat{\mathbf{n}}_{\mathrm{MX1}} = \pm \frac{(\mathbf{B}_{\mathrm{u}} \times \Delta\mathbf{V}) \times \Delta\mathbf{B}}{|(\mathbf{B}_{\mathrm{u}} \times \Delta\mathbf{V}) \times \Delta\mathbf{B}|} \tag{5}$$

$$\hat{\mathbf{n}}_{\mathrm{MX2}} = \pm \frac{(\mathbf{B}_{\mathrm{d}} \times \Delta\mathbf{V}) \times \Delta\mathbf{B}}{|(\mathbf{B}_{\mathrm{d}} \times \Delta\mathbf{V}) \times \Delta\mathbf{B}|} \tag{6}$$

$$\hat{\mathbf{n}}_{\mathrm{MX3}} = \pm \frac{(\Delta\mathbf{B} \times \Delta\mathbf{V}) \times \Delta\mathbf{B}}{|(\Delta\mathbf{B} \times \Delta\mathbf{V}) \times \Delta\mathbf{B}|} \tag{7}$$

where Δ represents the downstream to upstream difference, $\Delta\mathbf{A} \equiv \mathbf{A}_{\mathrm{d}} - \mathbf{A}_{\mathrm{u}}$ where $\mathbf{A}$ is any quantity, and the sign of the normal vector is taken such that the normal points from downstream towards upstream.

The magnetic coplanarity method, in (3), fails for $\theta_{\mathrm{Bn}} \to 90^\circ$ (and 0°) while the velocity coplanarity method, in (4), is an approximation only valid for high mach numbers and a θ_{Bn} close to 90° (or 0°) (Paschmann & Daly, 1998). The shock normals tabulated in Table 1 is calculated using the average of the three mixed methods in (5)-(7). However, one crossing exhibited an inconsistency between observation and calculated θ_{Bn}. This inconsistency, was the case for all methods except the Velocity coplanarity method. Hence, the Velocity coplanarity method was used for this crossing.

2.2.2 Shock velocity

Calculating the Mach numbers associated with a shock wave, the normal component of the upstream flow velocity relative to the shock (shock velocity), needs to be known. In order to determine the shock velocity, two methods are used: *the mass flux method* and *the Smith and Burton method*, for detailed descriptions of these methods see Pollock et al. (2016). *The mass flux method* gives the shock velocity as

$$V_{sh} = \frac{\Delta(n\mathbf{V})}{\Delta n} \cdot \hat{\mathbf{n}}. \tag{8}$$

This method requires good density (n) determination both upstream and downstream of the shock and information about the shock normal direction. *The Smith and Burton method* yields a shock velocity according to

$$V_{\mathrm{sh}} = \frac{|\Delta\mathbf{V} \times \mathbf{B}_{\mathrm{d}}|}{|\Delta\mathbf{B}|}. \tag{9}$$

This method does not require an explicit determination of the shock normal but rather a good velocity vector determination. The shock velocity used in the calculations is taken

as the average between the two methods. However, if one of the methods yields an unphysical velocity, such as shock velocity having a sign inconsistent with observations, then shock velocity from only one method is used.

2.2.3 Upstream shock parameters

The shock normal angle $\theta_{\rm Bn}$ is the angle between the upstream magnetic field $\mathbf{B}_{\rm u}$ and $\hat{\mathbf{n}}$,

$$\theta_{\rm Bn} = \arccos\left(\frac{\mathbf{B}_{\rm u}\cdot\hat{\mathbf{n}}}{|\mathbf{B}_{\rm u}|}\right). \tag{10}$$

From the data, $\theta_{\rm Bn}$ is estimated as the average using eq. (10) for the three different shock normals obtained via eqs. (5)-(7).

In the theory of astrophysical collisionless shocks, there are different Mach numbers governing the physics. The Alfvén Mach number $M_{\rm A}$ is the ratio of the normal component of the upstream flow velocity in the shock frame, $V_{\rm n,u}$, to the upstream Alfvén speed, $V_{\rm A}$. The fast magnetosonic Mach number can be calculated from the Alfvén Mach number and the total plasma beta using

$$M_{\rm ms} = \frac{V_{\rm n,u}}{\sqrt{V_{\rm A}^2 + C_{\rm s}^2}} = \frac{M_{\rm A}}{\sqrt{1+5\beta/6}} \tag{11}$$

where $C_{\rm s}$ is the sound speed and β is the total upstream plasma beta.

In this study, we will also consider two critical whistler Mach numbers. The linear whistler Mach number as defined in Balogh and Treumann (2013)

$$M_{\rm wh} = \frac{1}{2}\sqrt{\frac{m_{\rm i}}{m_{\rm e}}}|\cos\theta_{\rm Bn}| \tag{12}$$

depends only on the shock normal angle. For $M_{\rm A} < M_{\rm wh}$, whistler wave phase velocity can be going upstream away from the shock and thus allow the formation of standing wave fronts in front of quasi-perpendicular shocks. Eq. (12) is defined with respect to the whistler phase velocity. A similar expression for the linear whistler Mach number can be defined with respect to the group velocity instead, see e.g. Oka et al. (2017). Krasnoselskikh et al. (2002) also introduces a non-linear whistler Mach number ($M_{\rm whn}$), satisfying the equation

$$M_{\rm whn}^2(2M_{\rm wh}^2 - M_{\rm whn}^2)^3 = \beta_{\rm e}(2M_{\rm whn}^2 - M_{\rm wh}^2)^3, \tag{13}$$

that allows to find $M_{\rm whn}$ numerically. Unlike the linear one in (12), the nonlinear whistler Mach number not only depends on the shock angle but also has a weak dependence on

the electron plasma beta, β_e. For $M_A > M_{whn}$, all whistlers in front of the shock have group velocity downstream and are thus not able to stand in front of the quasi-perpendicular shock (Lalti et al., 2020).

2.3 Distribution function corrections

To make reliable estimates of the entropy and electron moments, the electron distribution functions that are downloaded from the MMS data archive have to be additionally calibrated. There are four corrections performed, all of them described below.

2.3.1 Spacecraft potential

Spacecraft has a potential Φ with respect to the ambient plasma environment, it is called spacecraft potential. Hence, a charged particle with energy E will be measured by MMS at a shifted energy

$$E' = E - q\Phi$$

where q is the charge of the particle. For a positive spacecraft potential, electrons will be accelerated by the spacecraft and measured at higher energies while protons (positive ions) will be decelerated and measured at lower energies. We correct the measured distribution functions by using the spacecraft potential estimates from the electric field instrument.

2.3.2 Secondary electrons

Secondary electron emissions contaminate the lower energy channels of the electron distribution functions measured by MMS, (Gershman et al., 2017). This contamination is illustrated in panel (a) of Figure 1. Figure 1 shows the electron distribution function average over all angles. The secondary electrons can be seen at low energies, $E < 20\,\mathrm{eV}$ as a fast increase in the distribution function when going to lower energies. The secondary electron number density increases with increasing background plasma density. This is attributed to secondary electron emissions due to background plasma electrons hitting the spacecraft and instrument surfaces.

In order to resolve the distribution function of the ambient background plasma, the low energy secondary electron population needs to be removed. This is done by modelling the secondary electron population as consisting of two components, one sun an-

gle dependent due to photoelectrons and one isotropic due to the ambient plasma. The sun angle dependent component is independent of the background ambient plasma density and is set according to Gershman et al. (2017), corresponding to a photoelectron density of $n_{\mathrm{ph}} = 0.35\,\mathrm{cm}^{-3}$. For the isotropic component, we construct a model described in more detail in Appendix B. This model is set to capture the secondary electron population's dependence on the ambient background plasma density. The secondary electron model distribution function is subtracted from the measured one of MMS according to

$$f_{\mathrm{e}} = f_{\mathrm{e,MMS}} - f_{\mathrm{ph}}.$$

The model distribution function, f_{ph}, is adjusted (see Appendix B) to yield a Maxwellian-like shape at the low energies for distributions (f_{e}) in the solar wind. For distributions (f_{e}) in the magnetosheath, the model distribution function, f_{ph}, is adjusted to resemble a flat top distribution. In panel (a) and (b) of Figure 1, the measured distribution functions and the corrected distribution functions are shown at five different shock crossing locations indicated in panel (c) of Figure 1.

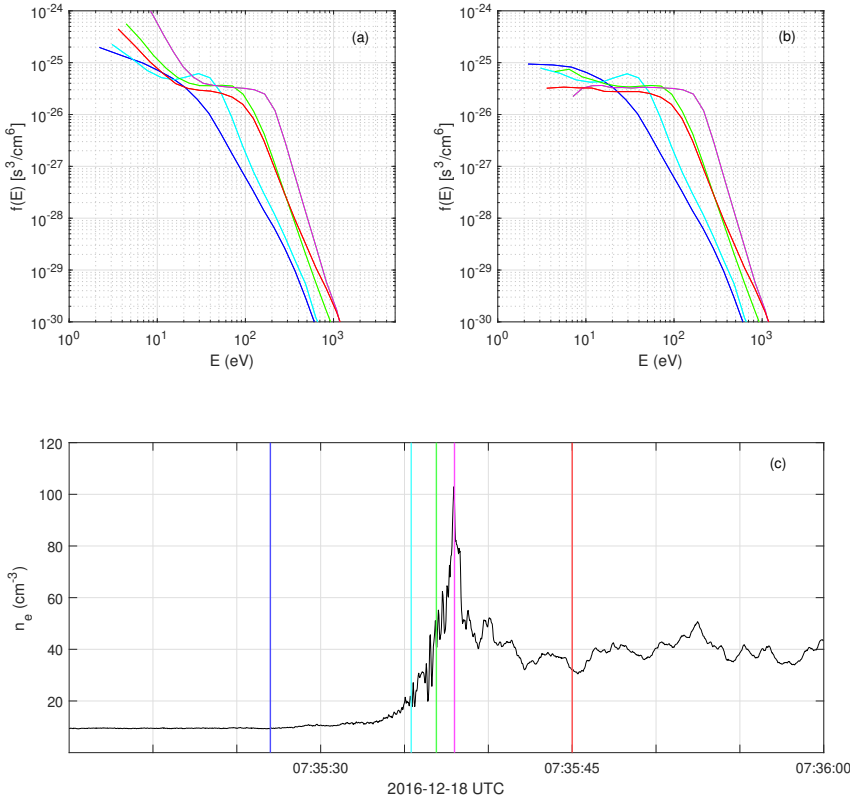

Figure 1. Distribution cuts showing the secondary electron contamination at the lower energies. Plot (a) and (b) shows the *uncorrected* resp. *corrected* distribution function cuts at five different times. These times are indicated by the colored vertical lines in plot (c) that shows the measured (MMS1) electron number density crossing the shock. The distributions in panel (a) and (b) have been averaged over a full solid angle. The calibration factors for this shock were $a = b = 1$ and the secondary electron models used for this shock were $n_{1,j}$ in solar wind and $n_{2,j}$ in the magnetosheath (see Appendix B and Table B1).

2.3.3 Extrapolation to zero energy

The part of the distributions ranging from the lowest energy bin value down to zero energy, while not measured by the spacecraft, it gives an important contribution to the entropy estimates. Therefore, it is important to use good approximations for the distribution function values in that interval. We assume that in the low energy range, the distribution of electrons is isotropic and the electron drift velocity is small compared to the thermal velocity. Based on this assumption we extrapolate the distribution functions down to zero as illustrated in Figure 2.

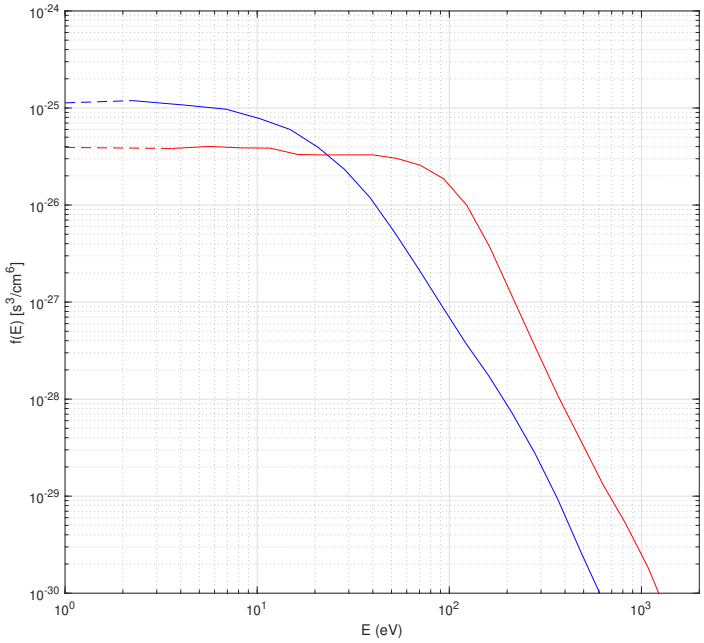

Figure 2. Distribution functions in upstream solar wind (blue) and downstream magnetosheath (red). The dashed lines indicate the extrapolated part of the distributions.

2.3.4 Density and Temperature

As a final step, the distribution function is calibrated such that it corresponds to the same density as obtained based on the measurements of plasma frequency f_{p} by the electric field instrument. We introduce a scale factor η such as $f_{\mathrm{new}} = \eta f_{\mathrm{old}}$ where f_{new} is the corrected distribution function and f_{old} is the original distribution function.

As an example, Figure 3 shows the electric field spectra of one shock crossing. The plasma frequency peak is seen in the upstream solar wind at roughly 30 kHz, corresponding to a plasma density of $n_{f_{\mathrm{p}}} \approx 11.3\,\mathrm{cm}^{-3}$. In this case all the corrections above provide a distribution function corresponding to a density of about $9.44\,\mathrm{cm}^{-3}$ and thus the scaling factor $\eta = 11.3/9.44 = 1.2$.

Figure 4 displays the difference between the measured and calculated electron density and temperature.

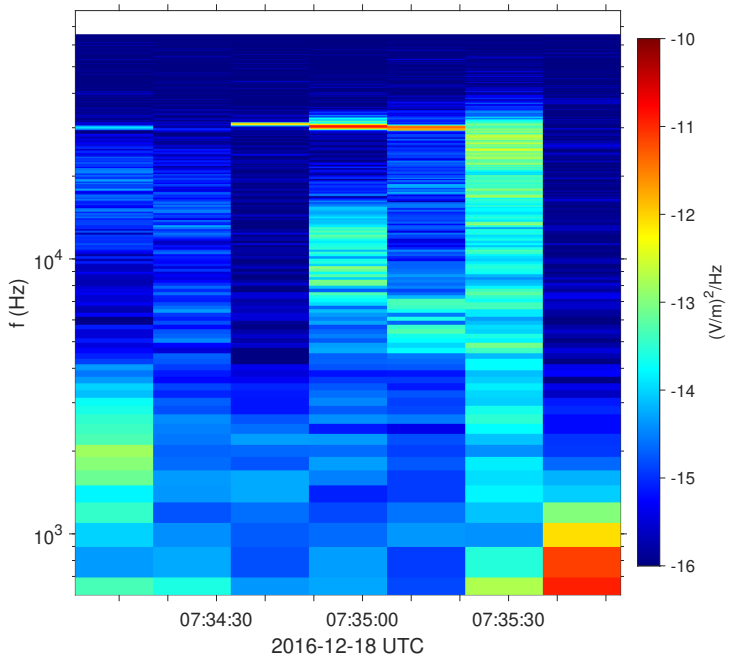

Figure 3. Electric field spectrogram for one shock crossing. The plasma frequency emission at $f \approx 30.1\,\mathrm{kHz}$ corresponds to a density of $11.3\,\mathrm{cm}^{-3}$.

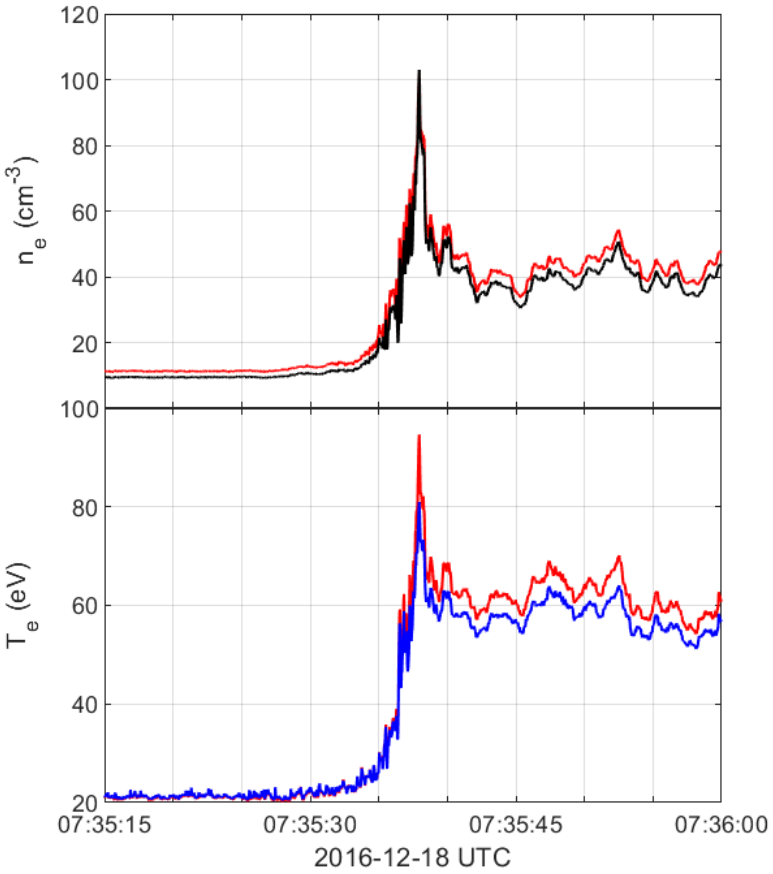

Figure 4. Comparison of the measured electron density (black) and electron temperature (blue) to the calculated ones (red). The red lines are calculated using the correction methods described in the method section.

2.4 Electron entropy calculation

The entropy density is calculated as

$$s = -k_{\mathrm{B}} \int f \ln(f) \mathrm{d}^3\mathbf{v} = s_0 - k_{\mathrm{B}} \sum_{i,j,k} f_{ijk} \ln(f_{ijk}) \Delta v_{ijk} \tag{14}$$

where Δv_{ijk} samples the phase space density volume element given in spherical coordinates as

$$\Delta v_{ijk} \propto \sqrt{(E_i - e\Phi)} \Delta E_i \sin\theta_j \Delta\theta_j \Delta\varphi_k. \tag{15}$$

s_0 is the extrapolated part of the distribution function (illustrated by the dashed lines in Figure 2). Assuming the distribution function is approximately constant at these en-

ergies, we obtain

$$s_0 = -k_{\mathrm{B}}\langle f \ln f\rangle \int_0^{E_0} \mathrm{d}^3\mathbf{v} = -k_{\mathrm{B}}\langle f \ln f\rangle \frac{8\pi E_0^{3/2}}{3} \tag{16}$$

where E_0 denotes the lower edge of the lowest electron energy bin and $\langle f \ln f\rangle$ is the mean of the (solid angle averaged) distribution function values at the two lowest energies. The entropy per particle, defined in eq. (2), is then obtained by dividing the entropy density by the calculated number density, $n = \int f \mathrm{d}^3\mathbf{v}$, obtained using the corrected distribution function.

3 Results

Figure 5 displays the shock event henceforth referred to as crossing 5. The first four top panels, (a)-(d), shows the magnetic field, ion velocity, ion differential energy flux and electron differential flux as measured by MMS1. Panels (e)-(g) shows the electron number density, electron temperature and electron kinetic entropy per particle calculated using the calibrated distribution function described in the previous section. The last panel, (h), shows the kinetic entropy of ions calculated directly from the measured ion distribution function from MMS1.

The data displayed in Figure 5 shows the characteristic signs of a quasi-perpendicular shock crossing. At the start of the interval, spacecraft are in the upstream solar wind. Around 07:35:27 UTC ion velocity starts to decrease and the spacecraft enter the foot region of the shock. The ion spectrogram shows a high energy ion population, associated to the shock, to be present already at 07:35:21 UTC. Hence, the solar wind upstream parameters are taken as averaged values before this time. At around 07:35:36 UTC, the MMS1 spacecraft measures a sharp increase in density and temperature. This increase coincides with a sharp transition in the ion and electron differential energy flux and is interpreted as the shock ramp. The sharp peak seen in the magnetic field, density and temperature at around 07:35:38 UTC is identified as the overshoot which is followed by the downstream magnetosheath. The calculated entropy (panels (g) and (h)) of the two species is observed to increase across the shock. We define upstream and downstream parameters by taking a 6 second average, 07:35:15-07:35:21 UTC upstream and 07:35:54-07:36:00 UTC downstream. The Alfvén Mach number of this shock is $M_{\mathrm{A}} \approx 10.9$ and the shock angle is $\theta_{\mathrm{Bn}} \approx 61°$. The change in electron entropy is $0.39k_{\mathrm{B}}$ and the change in ion entropy $2.9k_{\mathrm{B}}$. All the other shocks have been analyzed in a similar manner.

Tables 1, 2 and 3 show the shock parameters for the 22 analyzed crossings. The number, date and time of each shock is shown in Table 1 and referencing to a specific shock crossing will hereafter be done using their number. Also shown in Table 1 include, the averaged upstream values of the magnetic field, ion velocity, electron density, electron temperature and the shock normal in GSE-coordinates for each crossing.. Tables 2 and 3 show the change in electron entropy, ΔS_{e}, along with 10 other shock parameters including the fast magnetosonic Mach number, Alfvén Mach number, upstream electron plasma beta, shock angle, change in density, change in electron temperature, adiabatic index, linear and non-linear whistler Mach numbers and maximal electric field strength measured at the shock. The adiabatic index for electrons is calculated based on an analytical expression. Under the assumption of a calorically perfect gas (constant heat capacities), the change in entropy can be expressed as (Balogh & Treumann, 2013; Anderson, 2004)

$$\Delta S = k_{\mathrm{B}} \ln \left[\frac{N_{\mathrm{u}}}{N_{\mathrm{d}}} \left(\frac{T_{\mathrm{d}}}{T_{\mathrm{u}}} \right)^{\frac{1}{\gamma - 1}} \right] \tag{17}$$

where u denotes upstream and d downstream. Assuming (17) applies for the different plasma species separately, the adiabatic index γ_{e} for electrons can be decided for each shock crossing (see last column in Table 2). With 22 shock crossings analyzed, we perform a statistical study. In Figure 6, we present the ΔS_{e} plotted against the parameters listed above.

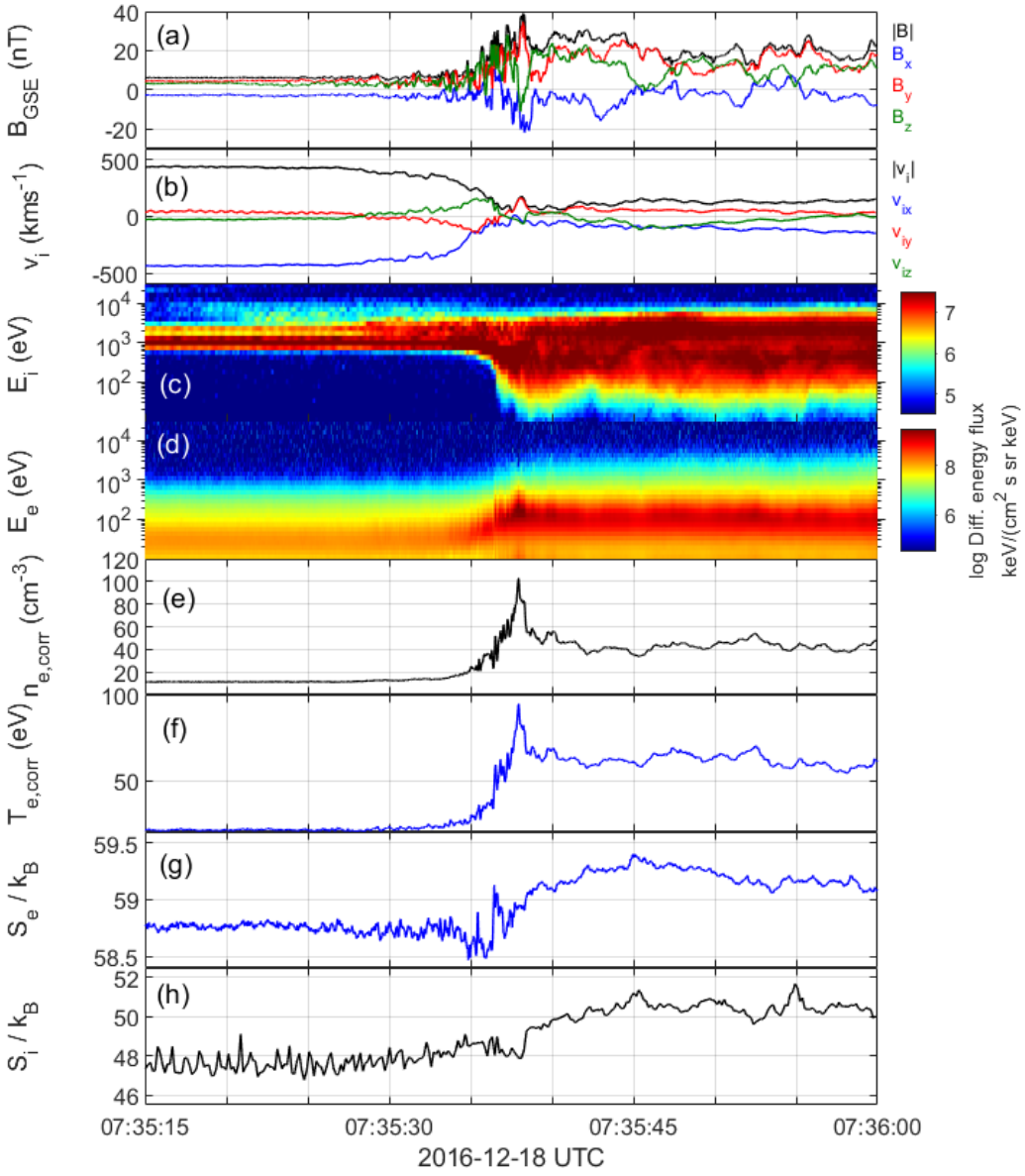

Figure 5. MMS1 measurements of shock crossing nr 5. It shows, (a) measured Magnetic field, (b) ion velocity, (c) ion spectrogram, (d) electron spectrogram, (e) calculated electron density, (f) calculated electron temperature, (g) electron kinetic entropy per particle and (h) ion kinetic entropy per particle.

Crossing	B_{u}[nT]	V_{u}[km/s]	$n_{\mathrm{e,u}}$[1/cc]	$T_{\mathrm{e,u}}$[eV]	$\hat{\mathbf{n}}$ (GSE)
1. 2016-11-10 17:10	12.4	379	24.1	19.2	0.88 0.44 0.18
2. 2016-11-10 16:59	7.0	373	43.8	17.3	0.81 0.58 0.07
3. 2016-12-06 10:55	8.0	343	24.8	11.6	0.97 0.24 0.02
4. 2016-12-09 10:29	7.9	617	6.9	13.0	0.99 0.15 -0.06
5. 2016-12-18 07:36	6.2	439	11.3	21.0	0.99 -0.09 0.03
6. 2017-01-01 09:11	3.9	486	9.2	16.5	0.99 -0.13 0.07
7. 2017-01-15 06:43	5.0	324	19.1	10.4	0.88 0.26 0.39
8. 2017-01-18 05:39	17.1	374	21.7	17.8	0.95 -0.32 0.003
9. 2017-01-31 10:07	9.1	645	11.0	16.4	0.94 -0.24 0.24
10. 2017-10-18 04:34	3.3	404	4.7	15.8	0.80 0.55 0.25
11. 2017-11-02 04:27	9.9	317	17.0	13.2	0.73 0.66 0.15
12. 2017-11-24 23:20	9.1	396	7.3	12.0	0.86 0.48 0.20
13. 2017-11-28 18:01	5.2	405	11.3	11.8	0.99 0.03 0.05
14. 2017-12-26 22:10	3.2	460	7.1	14.9	0.94 -0.07 0.33
15. 2018-01-24 04:05	2.4	369	5.9	9.8	0.92 -0.35 0.16
16. 2018-11-16 00:11	4.3	361	7.5	9.5	0.80 0.57 0.18
17. 2018-11-18 17:47	5.6	310	17.6	7.5	0.84 0.43 0.32
18. 2018-11-27 04:18	3.4	299	16.3	11.7	0.95 0.22 0.24
19. 2018-12-16 20:16	4.0	325	11.5	12.4	0.96 0.14 0.25
20. 2018-12-25 07:56	4.6	325	9.9	12.3	0.98 0.16 0.11
21. 2019-12-17 21:44	3.5	327	9.6	12.0	0.89 0.15 0.42
22. 2020-04-17 18:19	3.4	297	8.8	8.2	0.63 -0.78 -0.04

Table 1. The studied shock crossings along with the upstream parameters and calculated shock normal vectors. The upstream parameters are obtained taking a 6 second average. The shock normals are obtained as the average of the three mixed methods in (5)-(7) except for crossing 10 where the velocity coplanarity method was used.

Crossing	$M_{\rm ms}$	$M_{\rm A}$	$\beta_{\rm e}$	$\theta_{\rm Bn}$	$\Delta n/n_{\rm SW}$	$\Delta T_{\rm e}/T_{\rm e,SW}$	$\Delta S_{\rm e}/k_{\rm B}$	$\gamma_{\rm e}$
1	4.8	7.1	1.2	63	2.6	2.2	0.59	1.53
2	4.9	13.6	6.2	89	2.4	1.0	-0.06	1.65
3	4.4	7.9	1.8	79	3.0	2.2	0.51	1.62
4	6.0	9.9	0.6	89	3.7	5.3	1.44	1.62
5	5.4	10.9	2.5	61	2.7	1.8	0.39	1.64
6	5.1	14.7	4.0	64	2.5	1.4	0.31	1.63
7	5.0	10.5	3.3	89	2.4	1.3	0.10	1.63
8	3.8	4.8	0.5	59	2.3	2.5	0.75	1.61
9	5.4	10.8	0.9	77	3.3	4.4	1.27	1.62
10	3.6	7.1	2.8	59	2.5	1.2	0.10	1.63
11	3.1	4.4	0.9	64	2.4	1.6	0.27	1.61
12	3.8	4.6	0.4	84	3.9	3.6	1.30	1.60
13	6.2	11.3	2.0	75	3.5	3.0	0.71	1.57
14	5.8	15.5	4.1	84	2.8	1.8	0.62	1.57
15	8.1	18.2	4.1	79	3.9	2.0	0.50	1.62
16	5.1	8.2	1.5	83	3.2	2.8	0.90	1.60
17	4.5	7.8	1.7	70	4.7	2.1	0.12	1.60
18	5.0	13.7	6.7	67	2.0	0.83	-0.06	1.55
19	5.3	11.3	3.6	72	1.9	1.3	0.32	1.53
20	5.7	10.3	2.3	87	2.8	2.5	0.72	1.53
21	5.3	11.7	3.8	52	2.9	1.4	0.11	1.60
22	5.4	10.2	2.5	65	3.7	2.1	0.41	1.59

Table 2. The studied shock crossings along with the calculated fast magnetosonic Mach number, $M_{\rm ms}$, Alfvénic Mach number, $M_{\rm A}$, upstream electron plasma beta, $\beta_{\rm e}$, shock angle, $\theta_{\rm Bn}$, change in density, $\Delta n/n_{\rm SW}$, change in temperature, $\Delta T_{\rm e}/T_{\rm e,SW}$, change in electron entropy, $\Delta S_{\rm e}$ and adiabatic index, $\gamma_{\rm e}$.

Crossing	M_A/M_{wh}	M_A/M_{whn}	$\|E\|_{max}$[mV/m]	$\Delta S_e/k_B$
1	0.74	0.56	739	0.59
2	1.2	1.01	224	-0.06
3	1.9	1.6	178	0.51
4	44	29	121	1.44
5	1.05	0.85	271	0.39
6	1.5	1.2	121	0.31
7	28	34	130	0.10
8	0.44	0.34	716	0.75
9	2.2	2.3	192	1.27
10	0.42	0.33	117	0.10
11	0.47	0.37	143	0.27
12	2.0	2.7	482	1.30
13	2.1	1.8	294	0.71
14	7.2	7.2	82	0.62
15	4.4	4.1	261	0.50
16	3.4	2.6	203	0.90
17	1.06	0.82	293	0.12
18	1.6	1.4	194	-0.06
19	1.7	1.5	441	0.32
20	8.6	8.8	302	0.72
21	0.88	0.72	171	0.11
22	1.12	0.93	231	0.41

Table 3. The studied shock crossings with Alfvénic to whistler mach number ratio(s) (linear and non-linear), maximum electric field strength measured across the shock and electron kinetic entropy change.

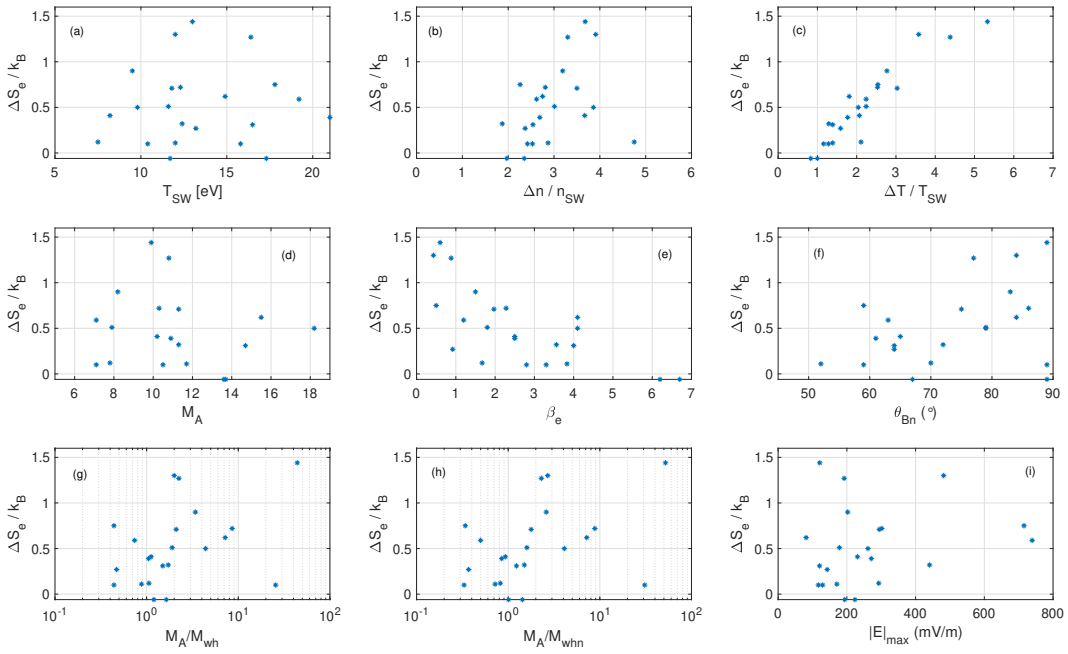

Figure 6. The change in kinetic electron entropy per particle (ΔS_e) plotted against (a) solar wind electron temperature, (b) difference in electron number density, (c) difference in electron temperature, (d) Alfvénic Mach number, (e) electron plasma beta, (f) shock normal angle, (g) Alfvénic to linear whistler Mach number ratio, (h) Alfvénic to non-linear whistler Mach number ratio and (i) maximum electric field strength measured crossing the shocks.

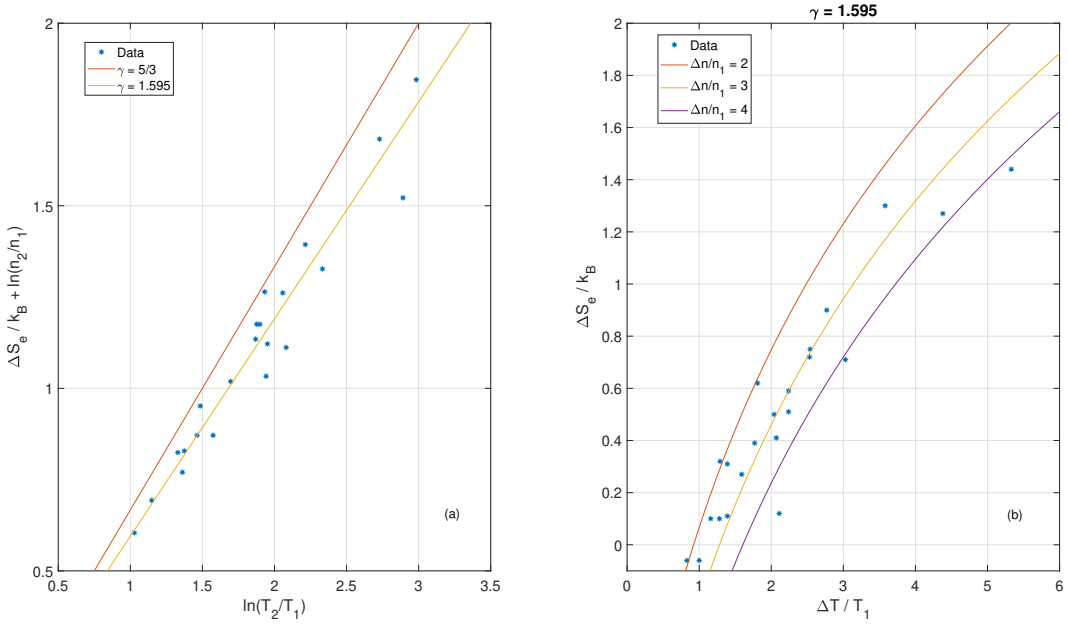

Figure 7. The average adiabatic index for electrons of all 22 shock crossings is calculated to be $\gamma_e = 1.595 \pm 0.036$. Panel (a) shows how this value fit our data better than the $\gamma = 5/3$, which is that for an ideal gas. Panel (b) displays the change in entropy vs change in temperature (blue asterisks) and the analytical expression in (17) for the same at four different density ratios with $\gamma_e = 1.595$. Here index 1 stands for solar wind and 2 for magnetosheath.

4 Discussion

Studying Table 2, crossing the shock from upstream to downstream, the kinetic entropy increases in nearly all of the crossings, except two that are discussed in the next paragraph. With energy being dissipated at the shock, an increase of entropy is expected (Balogh & Treumann, 2013). Collisionless shocks generating entropy has been reported by Cluster in Parks et al. (2012). However, we find that the $\Delta S_e \approx 2k_B$ stated by Parks et al. (2012) is not observed in this study. Instead, the change in electron entropy is find to vary between $-0.06k_B$ and $1.4k_B$ with an average of $\langle \Delta S_e \rangle = 0.51k_B$.

Crossing 2 and 18 display a $\Delta S_e \approx -0.06 < 0$, *i.e.* the entropy seems to decrease across the shock. Note that the change is rather close to zero so this might be due to numerical effects and/or left over photoelectrons. That is, if the real change in entropy is positive but close to zero, any small left over part of photoelectrons could make the calculated ΔS negative.

Studying Figure 6, we note a clear trend in panel (c) between the ΔS_e and the ΔT_e. This is expected due to energy dissipating processes occurring at the shock (Balogh & Treumann, 2013). Irreversible processes always increase entropy and temperature (Blundell & Blundell, 2010), hence we expect an increase in entropy to yield an increase in temperature. We also observe a trend in panel (e), between the ΔS_e and the electron plasma beta, β_e. A high ΔS_e is associated with a low solar wind electron plasma beta, $\beta_\mathrm{e} < 1$. While a low ΔS_e is associated with a high solar wind electron plasma beta, $\beta_\mathrm{e} > 1$. This inverse electron beta-dependence is qualitatively similar to what is theoretically predicted for the *total* entropy per particle change vs the *total* plasma beta across a collisionless shock assuming a one fluid MHD approximation, see Appendix A and Figure A2.

For the other parameters in Figure 6 (not panel (c) or (e)), no clear trend is observed and more crossings need to be analyzed. Due to the strong ΔS_e-dependence on the electron plasma β_e, we suggest the other parameters to be analyzed using a limited range of electron plasma β_e.

We find the average adiabatic index for all shocks to be $\langle \gamma_\mathrm{e} \rangle \approx 1.595$ with a standard deviation of 0.036. This is compared to the value for a monoatomic gas with 3 degrees of freedom , $\gamma = 5/3$ (Anderson, 2004), in Figure 7. Comparing the (b) panels of Figure 6 and 7, states that the change in electron entropy follow the expression in (17) quite well for an adiabatic index of $\gamma_\mathrm{e} \approx 1.595 \pm 0.036$.

The Maxwellian distribution represents the maximum state of entropy and using the definition of kinetic entropy density in (1), an analytical expression can be found for a given plasma density, n, and temperature, T, (Liang et al., 2020)

$$s_M = \frac{3}{2} k_\mathrm{B} n \left[1 + \ln \left(\frac{2\pi k_\mathrm{B} T}{m n^{2/3}} \right) \right]. \tag{18}$$

Figure 8 depicts a comparison between the entropy per particle (eq. (18) divided by n) of a Maxwellian distribution and the entropy calculated using MMS. As expected, the calculated entropy is strictly less then the maximum state (Maxwellian) throughout the interval. Studying the difference between the two in Figure 8, we note that the plasma is not completely thermalized in the magnetosheath. However, the calculated entropy in the magnetosheath is closer to the maximum entropy state (Maxwellian) compared to the entropy measured in the solar wind. This comparison was made for crossing 1-9, 12 and 22 and similar behavior was observed for all.

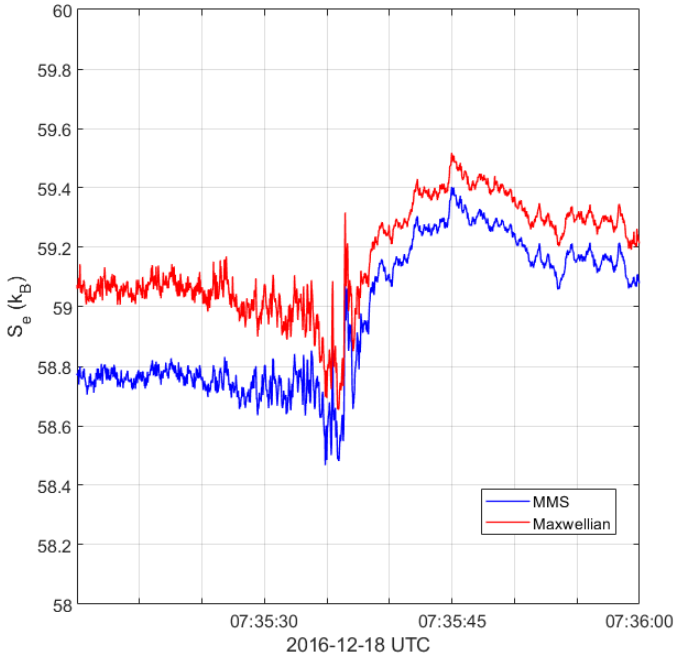

Figure 8. Comparison of the calculated entropy (blue) to the entropy of a Maxwellian distribution (red).

5 Conclusion

We use MMS-data to calculate the kinetic entropy per particle across Earth's quasi-perpendicular bow shock. 22 quasi-perpendicular shock crossings have been analyzed. The kinetic entropy per particle is calculated using the kinetic definition of entropy via the measured distribution function of MMS1. It is shown that the measured electron distribution function needs further calibrations when calculating the entropy and plasma moments such as density and temperature. The calibrations are presented and described in the method section. Our main findings are:

- 20 out of 22 crossings display an increase in the electron kinetic entropy ranging between $\Delta S_\mathrm{e} \approx 0.1 - 1.4 k_\mathrm{B}$.
- Two crossings display a slight decrease $\Delta S_\mathrm{e} \approx -0.06 k_\mathrm{B}$.
- The measured/calculated electron entropy per particle of 11 crossings are compared to the entropy per particle of a Maxwellian distribution. We find the measured entropy to be strictly less than the Maxwellian's for all 11 shocks. We note that the plasma is not completely thermalized in the magnetosheath. However,

the calculated entropy in the magnetosheath is closer to the maximum entropy state (Maxwellian) compared to the entropy measured in the solar wind.

- We observe that the ΔS_e displays a strong dependence on the change in electron temperature across the shock, ΔT_e, and the upstream electron plasma beta, β_e. Shocks with high ΔT_e are found to have high ΔS_e. Shocks with low upstream electron plasma betas are found to generate more entropy than shocks with large electron plasma beta.
- For the parameters, M_A, M_{wh}, M_{whn}, T_{SW}, Δn_e and E_{max} no clear trend is observed and more crossings need to be analyzed.
- The adiabatic index of electrons is calculated for each shock using the analytical expression in eq. (17). The index best describing our data is determined to be $\gamma_e = 1.595$ with a standard deviation of 0.036.

Acknowledgments

We thank the entire MMS team for data access and support. The MMS data are available at the MMS Science Data Center (https://lasp.colorado.edu/mms/sdc). The OMNI data were obtained from the GSFC/SPDF OMNIWeb interface at https://omniweb.gsfc.nasa.gov. A special thanks to Daniel Graham, Yuri Khotyaintsev, Ahmad Lalti and Wenya Li for valuable discussions contributing to the development of this work. Data analysis was performed using the IRFU-Matlab analysis package. This work is supported by the Swedish Research Council grant 2018-05514.

Appendix A Analytical calculation of total entropy change across collisionless shock

This section provides a theoretical prediction of the change in total entropy per particle as a function of the upstream parameters of a shock in a single fluid approximation. Starting from the Rankine-Hugoniot equations, the density and temperature ratios can be determined solely by the upstream Alfvénic Mach number M_A, shock angle θ_{Bn} and upstream total plasma beta β_1.

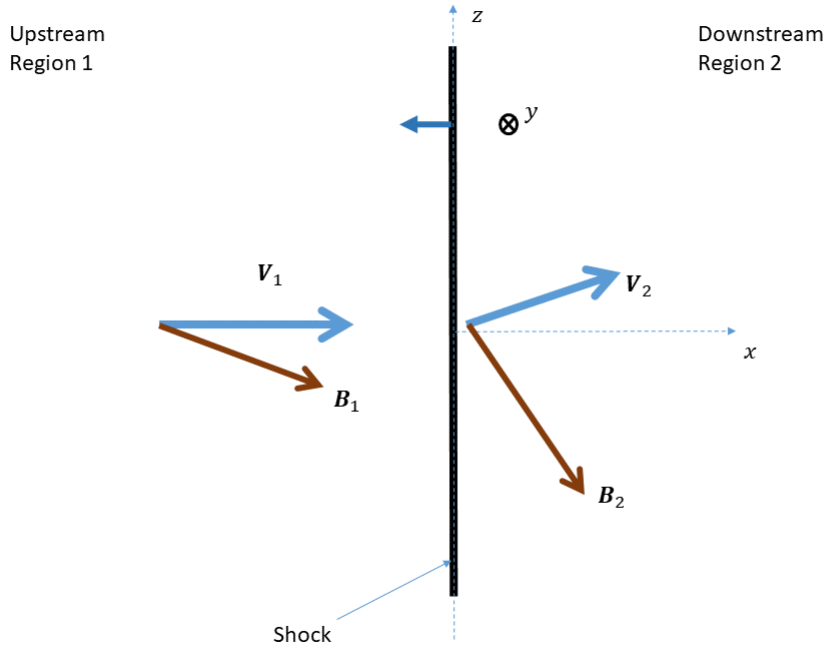

Figure A1. The 1D shock geometry assumed. Picture taken from Balogh and Treumann (2013).

The Rankine-Hugoniot equations are given by Kivelson and Russel (1995):

$$\hat{\mathbf{n}} \cdot \{\mathbf{B}\} = 0$$

$$\hat{\mathbf{n}} \cdot \{N\mathbf{V}\} = 0$$

$$\{\hat{\mathbf{n}} \times (\mathbf{V} \times \mathbf{B})\} = \mathbf{0}$$

$$\hat{\mathbf{n}} \cdot \{mN\mathbf{V}\mathbf{V}\} + \hat{\mathbf{n}}\left\{P + \frac{B^2}{2\mu_0}\right\} - \frac{1}{\mu_0}\hat{\mathbf{n}} \cdot \{\mathbf{B}\mathbf{B}\} = \mathbf{0}$$

$$\left\{mN\hat{\mathbf{n}} \cdot \mathbf{V}\left[\frac{V^2}{2} + w + \frac{1}{mN}\left(P + \frac{B^2}{\mu_0}\right)\right] - \frac{1}{\mu_0}(\mathbf{V} \cdot \mathbf{B})\hat{\mathbf{n}} \cdot \mathbf{B}\right\} = 0$$

For an ideal gas we have

$$P = Nk_BT$$

and enthalpy per mass

$$h = w + \frac{P}{\rho} = \frac{C_pT}{m}.$$

This gives

$$\hat{\mathbf{n}} \cdot \{\mathbf{B}\} = 0 \tag{A1}$$

$$\hat{\mathbf{n}} \cdot \{N\mathbf{V}\} = 0 \tag{A2}$$

$$\{\hat{\mathbf{n}} \times (\mathbf{V} \times \mathbf{B})\} = \mathbf{0} \tag{A3}$$

$$\hat{\mathbf{n}} \cdot \{mN\mathbf{V}\mathbf{V}\} + \hat{\mathbf{n}}\left\{Nk_BT + \frac{B^2}{2\mu_0}\right\} - \frac{1}{\mu_0}\hat{\mathbf{n}} \cdot \{\mathbf{B}\mathbf{B}\} = \mathbf{0} \tag{A4}$$

$$\left\{mN\hat{\mathbf{n}} \cdot \mathbf{V}\left(\frac{V^2}{2} + \frac{C_pT}{m} + \frac{B^2}{\mu_0 mN}\right) - \frac{1}{\mu_0}(\mathbf{V} \cdot \mathbf{B})\hat{\mathbf{n}} \cdot \mathbf{B}\right\} = 0 \tag{A5}$$

From Figure A1, we get

$$\mathbf{V}_1 = V_1\hat{\mathbf{n}}$$

$$\mathbf{B}_1 = (B_n, 0, B_{z1})$$

$$\mathbf{V}_2 = (V_{n2}, 0, V_{z2})$$

$$\mathbf{B}_2 = (B_n, 0, B_{z2})$$

where (A1) above yields $B_{n1} = B_{n2} = B_n$ and have been used.

Using the above assumptions, (A2) above yields

$$N_2V_{n2} = N_1V_1$$

$\Rightarrow$

$$\boxed{\frac{N_2V_{n2}}{N_1V_1} = 1} \tag{A6}$$

Using the vector identity, $\mathbf{A} \times (\mathbf{B} \times \mathbf{C}) = \mathbf{B}(\mathbf{A} \cdot \mathbf{C}) - \mathbf{C}(\mathbf{A} \cdot \mathbf{B})$, on (A3) yields

$$\mathbf{V}_2(\hat{\mathbf{n}} \cdot \mathbf{B}_2) - \mathbf{B}_2(\hat{\mathbf{n}} \cdot \mathbf{V}_2) = \mathbf{V}_1(\hat{\mathbf{n}} \cdot \mathbf{B}_1) - \mathbf{B}_1(\hat{\mathbf{n}} \cdot \mathbf{V}_1)$$

which then gives

$$\mathbf{V}_2B_n - \mathbf{B}_2V_{n2} = \hat{\mathbf{n}}V_1B_n - \mathbf{B}_1V_1.$$

The normal component gives nothing of value while the z-component yields:

$$B_{z2}V_{n2} - V_{z2}B_n = B_{z1}V_1.$$

This gives

$$\boxed{B_{z2}\frac{V_{n2}}{V_1} - \frac{V_{z2}}{V_1}B_n = B_{z1}} \tag{A7}$$

Consider now the z-component of (A4)

$$mN_2V_{n2}V_{z2} - \frac{1}{\mu_0}B_nB_{z2} = -\frac{1}{\mu_0}B_nB_{z1}$$

using (A6) gives

$$\frac{1}{\mu_0}B_nB_{z2} - mN_1V_1V_{z2} = \frac{1}{\mu_0}B_nB_{z1}$$

and divide through with $mN_1V_1^2$ yields:

$$\boxed{\frac{B_nB_{z2}}{\mu_0 mN_1V_1^2} - \frac{V_{z2}}{V_1} = \frac{B_nB_{z1}}{\mu_0 mN_1V_1^2}} \tag{A8}$$

Consider now the normal component of (A4)

$$mN_2V_{n2}^2 + N_2k_BT_2 + \frac{B_n^2+B_{z2}^2}{2\mu_0} - \frac{1}{\mu_0}B_n^2 = mN_1V_1^2 + N_1k_BT_1 + \frac{B_n^2+B_{z1}^2}{2\mu_0} - \frac{1}{\mu_0}B_n^2$$

using (A6) again and canceling some terms gives

$$mN_1V_1V_{n2} + N_2k_BT_2 + \frac{B_{z2}^2}{2\mu_0} = mN_1V_1^2 + N_1k_BT_1 + \frac{B_{z1}^2}{2\mu_0}$$

Divide through by $mN_1V_1^2/2$

$$\boxed{2\frac{V_{n2}}{V_1} + 2\frac{N_2k_BT_2}{mN_1V_1^2} + \frac{B_{z2}^2}{\mu_0 mN_1V_1^2} = 2 + 2\frac{k_BT_1}{mV_1^2} + \frac{B_{z1}^2}{\mu_0 mN_1V_1^2}} \tag{A9}$$

Finally, eq. (A5) becomes:

$$mN_2V_{n2}\left(\frac{V_{n2}^2+V_{z2}^2}{2} + \frac{C_pT_2}{m} + \frac{B_n^2+B_{z2}^2}{\mu_0 mN_2}\right) - \frac{1}{\mu_0}(V_{n2}B_n + V_{z2}B_{z2})B_n =$$

$$= mN_1V_1\left(\frac{V_1^2}{2} + \frac{C_pT_1}{m} + \frac{B_n^2+B_{z1}^2}{\mu_0 mN_1}\right) - \frac{V_1B_n^2}{\mu_0}$$

Divide through by mN_1V_1 and make use of (A6)

$$\frac{V_{n2}^2+V_{z2}^2}{2} + \frac{C_pT_2}{m} + \frac{B_n^2+B_{z2}^2}{\mu_0 mN_2} - \frac{B_n}{\mu_0 mN_1V_1}(V_{n2}B_n + V_{z2}B_{z2}) =$$

$$= \frac{V_1^2}{2} + \frac{C_pT_1}{m} + \frac{B_n^2+B_{z1}^2}{\mu_0 mN_1} - \frac{B_n^2}{\mu_0 mN_1}$$

now divide through by $V_1^2/2$

$$\frac{V_{n2}^2+V_{z2}^2}{V_1^2} + 2\frac{C_pT_2}{mV_1^2} + 2\frac{N_1}{N_2}\frac{B_n^2+B_{z2}^2}{\mu_0 mN_1V_1^2} - \frac{2B_n}{\mu_0 mN_1V_1^3}(V_{n2}B_n + V_{z2}B_{z2}) =$$

$$= 1 + 2\frac{C_pT_1}{mV_1^2} + \frac{2B_{z1}^2}{\mu_0 mN_1V_1^2} \tag{A10}$$

Introducing the normalized parameters

$$\frac{N_2}{N_1} \to N_2 \quad , \quad \frac{\mathbf{V}_2}{V_1} \to \mathbf{V}_2 \quad , \quad \frac{\mathbf{B}_i}{V_1\sqrt{\mu_0 mN_1}} \to \mathbf{B}_i \quad , \quad \frac{k_BT_i}{mV_1^2} \to T_i \tag{A11}$$

equations (A6)-(A10) can be written as

$$N_2 V_{n2} = 1$$

$$B_{z2} V_{n2} - V_{z2} B_n = B_{z1}$$

$$B_n B_{z2} - V_{z2} = B_n B_{z1}$$

$$2V_{n2} + 2N_2 T_2 + B_{z2}^2 = 2(1 + T_1) + B_{z1}^2$$

$$V_{n2}^2 + V_{z2}^2 + \frac{2\gamma T_2}{\gamma - 1} + \underbrace{2V_{n2}B_{z2}^2 - 2V_{z2}B_n B_{z2}}_{2B_{z1}B_{z2}} = 1 + \frac{2\gamma T_1}{\gamma - 1} + 2B_{z1}^2$$

where (A6) have been used on the third term in (A10) to yield the last equation and then eq. (A13) in the underbrace.

We end up with

$$N_2 V_{n2} = 1 \tag{A12}$$

$$B_{z2} V_{n2} - V_{z2} B_n = B_{z1} \tag{A13}$$

$$B_n B_{z2} - V_{z2} = B_n B_{z1} \tag{A14}$$

$$2N_2(V_{n2}^2 + T_2) + B_{z2}^2 = 2(1 + T_1) + B_{z1}^2 \tag{A15}$$

$$V_{n2}^2 + V_{z2}^2 + \frac{2\gamma T_2}{\gamma - 1} + 2B_{z1}B_{z2} = 1 + \frac{2\gamma T_1}{\gamma - 1} + 2B_{z1}^2 \tag{A16}$$

A1 Solve for V_{n2}

Using the adiabatic index, γ, equal to 5/3 (Anderson, 2004) and performing the following operations:

- Solve for V_{z2} in (A14).
- Solve for B_{z2} in (A13).
- Mult. (A15) with $5V_{n2}/2$ and make use of (A12).
- Add $4V_{n2}^2$ to (A16)

and we end up with:

$$V_{z2} = B_n(B_{z2} - B_{z1}) \tag{A17}$$

$$B_{z2} = \frac{B_{z1}(B_n^2 - 1)}{B_n^2 - V_{n2}} \tag{A18}$$

$$5(V_{n2}^2 + T_2) + \frac{5}{2}V_{n2}B_{z2}^2 = 5V_{n2}(1 + T_1) + \frac{5}{2}V_{n2}B_{z1}^2 \tag{A19}$$

$$5(V_{n2}^2 + T_2) + V_{z2}^2 + 2B_{z1}B_{z2} = 1 + 5T_1 + 2B_{z1}^2 + 4V_{n2}^2 \tag{A20}$$

Subtract (A20) to (A19) in order to eliminate T_2

$$V_{z2}^2 + 2B_{z1}B_{z2} - \frac{5}{2}V_{n2}B_{z2}^2 = 1 + 5T_1 + 2B_{z1}^2 + 4V_{n2}^2 - 5V_{n2}(1+T_1) - \frac{5}{2}V_{n2}B_{z1}^2$$

and perform the following steps:

- Insert expression (A17), eliminating V_{z2}.
- Insert expression (A18), eliminating B_{z2}.
- Multiply the whole equation with $(B_n^2 - V_{n2})^2$.

The above steps yields the following equation for V_{n2}

$$a_4 V_{n2}^4 + a_3 V_{n2}^3 + a_2 V_{n2}^2 + a_1 V_{n2} + a_0 = 0 \tag{A21}$$

where the coefficients are given by

$$\begin{aligned}
a_0 &= B_n^2[\mathbf{B}_1^2 + 5B_n^2 T_1] && \text{(A22)}\\
a_1 &= \frac{1}{2}B_{z1}^2 - B_n^2[2 + 5\mathbf{B}_1^2 + 5T_1(2 + B_n^2)] && \text{(A23)}\\
a_2 &= 1 + 5T_1 + 2B_{z1}^2 + 2B_n^2[5 + 2\mathbf{B}_1^2 + 5T_1] && \text{(A24)}\\
-a_3 &= 5 + 8B_n^2 + \frac{5}{2}B_{z1}^2 + 5T_1 && \text{(A25)}\\
a_4 &= 4 && \text{(A26)}
\end{aligned}$$

We see that the solution for V_{n2} in (A21) will depend on the upstream parameters B_n, B_{z1} and T_1. Using the Normalization in (A11), these parameters can be expressed as

$$\begin{aligned}
\mathbf{B}_1^2 &= \tfrac{1}{M_A^2} && \text{(A27)}\\
B_n &= \tfrac{\cos\theta_{Bn}}{M_A} && \text{(A28)}\\
B_{z1} &= \tfrac{\sin\theta_{Bn}}{M_A} && \text{(A29)}\\
T_1 &= \tfrac{\beta_1}{2M_A^2} && \text{(A30)}
\end{aligned}$$

and (A22)-(A26) can be expressed as

$$\begin{aligned}
a_0 &= \frac{(2M_A^2 + 5\beta_1\cos^2\theta_{Bn})\cos^2\theta_{Bn}}{2M_A^6} && \text{(A31)}\\
a_1 &= \frac{M_A^4 - 5\beta_1\cos^4\theta_{Bn} - 5M_A^2(2 + 2\beta_1 + M_A^2)}{2M_A^6} && \text{(A32)}\\
a_2 &= \frac{(8 + 10\beta_1 + 16M_A^2)\cos^2\theta_{Bn} + M_A^2(4 + 5\beta_1 + 2M_A^2)}{2M_A^4} && \text{(A33)}\\
-a_3 &= \frac{5 + 5\beta_1 + 10M_A^2 + 11\cos^2\theta_{Bn}}{2M_A^2} && \text{(A34)}\\
a_4 &= 4 && \text{(A35)}
\end{aligned}$$

A2 Temperature Ratio

Divide (A16) with $2c_pT_1$, where $c_p = \gamma/(\gamma-1)$:

$$\frac{V_{n2}^2}{2c_pT_1} + \frac{V_{z2}^2}{2c_pT_1} + \frac{T_2}{T_1} + \frac{2B_{z1}B_{z2}}{2c_pT_1} = \frac{1}{2c_pT_1} + 1 + \frac{2B_{z1}^2}{2c_pT_1}$$

Solve for T_2/T_1:

$$\frac{T_2}{T_1} = 1 + \frac{1}{2c_pT_1}\left[1 - V_{n2}^2 + \underbrace{2B_{z1}^2 - 2B_{z1}B_{z2}}_{-2B_{z1}V_{z2}/B_n} - V_{z2}^2\right]$$

Insert

$$V_{z2} = \frac{B_{z1}B_n(V_{n2}-1)}{(B_n^2 - V_{n2})}$$

which is obtained through (A18) in (A17). We obtain

$$\boxed{\frac{T_2}{T_1} = 1 + \frac{\gamma-1}{2\gamma T_1}\left[1 - V_{n2}^2 - \frac{2B_{z1}^2(V_{n2}-1)}{(B_n^2 - V_{n2})} - \frac{B_{z1}^2B_n^2(V_{n2}-1)^2}{(B_n^2 - V_{n2})^2}\right]} \tag{A36}$$

where B_n, B_{z1} and T_1 is given by the upstream parameters θ_{Bn}, M_A and β_1 in (A28), (A29) and (A30). Hence, using eq. (17), the total entropy change can be calculated via the upstream parameters θ_{Bn}, M_A and β_1 by deciding $V_{n2} = N_1/N_2$ numerically from (A21) and T_2/T_1 from (A36). The result is illustrated in Figure A2.

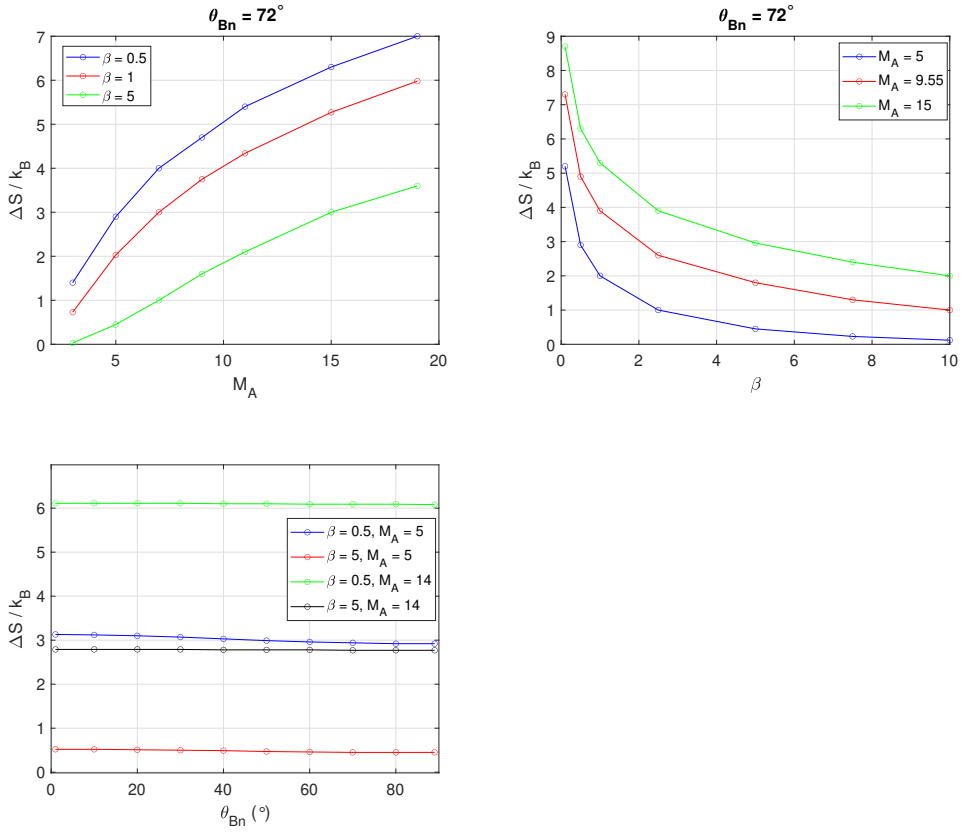

Figure A2. Theoretical prediction of total entropy change across collisionless shock in a one fluid plasma approximation.

Appendix B Secondary electron model across shock

In order to resolve the distribution function of the ambient background plasma, the low energy secondary electron population needs to be removed. This is done by modelling the secondary electron population as consisting of two components, one sun angle dependent due to the photoelectrons and one isotropic due to the ambient plasma. The sun angle dependent component is independent of the background ambient plasma density and is set according to Gershman et al. (2017), corresponding to a photoelectron density of $n_{\mathrm{ph}} = 0.35\,\mathrm{cm}^{-3}$. The isotropic component is estimated by examining partial densities associated with the shock crossings. We define the partial density $n(E)$ to be the number of electrons per cubic centimeter with energy E. Figure B1 shows partial densities, $n(E)$, at four different locations during a shock transition. This figure nicely illustrates the ambient plasma population (large peak) and the photoelectron population (portion of a small peak) at the low energies. In order to capture the density de-

pendence of the isotropic component, the total secondary electron density (photo and secondary electrons) is estimated using five simple models using the low energy region of the partial densities.

For each measured data point, j, in the shock time interval, let:

- $n_{0,j} = n_{\mathrm{ph}}$
- $n_{1,j} =$ Partial density value at the lowest energy
- $n_{2,j} =$ Sum of the two partial density values at the two lowest energies
- $n_{01,j} =$ Average between $0\,\mathrm{cm}^{-3}$ and $n_{1,j}$
- $n_{12,j} =$ Average between $n_{1,j}$ and $n_{2,j}$

where $n_{0,j}$ is set equal to the photoelectron density to represent a case with zero secondary electron density (see eq. (B1) below).

As an example, consider the data point (time) given by the red vertical line in panel (e) of Figure B1. The partial density corresponding to this line is seen in panel (d) of Figure B1 and evaluating the five models above yields:

$$
\begin{aligned}
n_0 &= 0.35\,\mathrm{cm}^{-3} \\
n_1 &\approx 3\,\mathrm{cm}^{-3} \\
n_2 &\approx 3\,\mathrm{cm}^{-3} + 1.9\,\mathrm{cm}^{-3} = 4.9\,\mathrm{cm}^{-3} \\
n_{01} &= \frac{0\,\mathrm{cm}^{-3} + 3\,\mathrm{cm}^{-3}}{2} = 1.5\,\mathrm{cm}^{-3} \\
n_{12} &= \frac{3\,\mathrm{cm}^{-3} + 4.9\,\mathrm{cm}^{-3}}{2} = 3.95\,\mathrm{cm}^{-3}
\end{aligned}
$$

This is done for all data points in the shock time interval. To pin point which two of the five options above to use (one in solar wind and one in magnetosheath) for each crossing, the flat top condition is used in the magnetosheath region and a Maxwellian condition for the solar wind region. To further improve the model, we introduce calibration factors a and b. In this way, the secondary electron density is expressed as

$$N_{\mathrm{SW},j} = a n_{\mathrm{SW},j} - n_{\mathrm{ph}} \tag{B1}$$

and

$$N_{\mathrm{MSh},j} = b n_{\mathrm{MSh},j} - n_{\mathrm{ph}} \tag{B2}$$

where $n_{\mathrm{SW},j}$ and $n_{\mathrm{MSh},j}$ is one of (not necessary the same) $[n_{0,j}, n_{01,j}, n_{1,j}, n_{12,j}, n_{2,j}]$ defined above , a and b are numbers close to 1 and the sun angle dependent photoelectron density have been subtracted.

We take crossing 5 as an example. Distributions in the solar wind were compared to a Maxwellian distribution with 6 second upstream temperature average and density obtained from plasma frequency electric field measurements. The secondary electron density in (B1) giving the best resemblance of the Maxwellian at the lower energies was found using $n_{\mathrm{SW},j} = n_{1,j}$ and $a = 1.0$. Distributions in the magnetosheath were assumed to be of flat top kind. The secondary electron density in (B2) best resembling flat top distributions was found using $n_{\mathrm{MSh},j} = n_{2,j}$ and $b = 1.0$.

B1 Transition region

Equation (B1) estimates the secondary electron number density needed to give a Maxwellian-like shape at the lower energies in the solar wind. (B2) estimates the secondary electron number density needed to give a flat top distribution in the magnetosheath. The shock being the boundary region between the solar wind and magnetosheath, we propose a gradual transition between the two models in (B1) and (B2) by using the following expression

$$N_{\mathrm{ramp},j} = \frac{(N-j)N_{\mathrm{SW},j} + (j-1)N_{\mathrm{MSh},j}}{N-1} \tag{B3}$$

for each data point j. The concept is illustrated in Figure B2 below.

The transition region interval is decided manually by eye for each shock crossing.

The resulting distribution functions, using the above described method for removing contaminating secondary electrons, can be seen in panel (b) of Figure 1. The resulting partial densities (removing the photo-electrons) are seen in panel (a)-(d) in Figure B1.

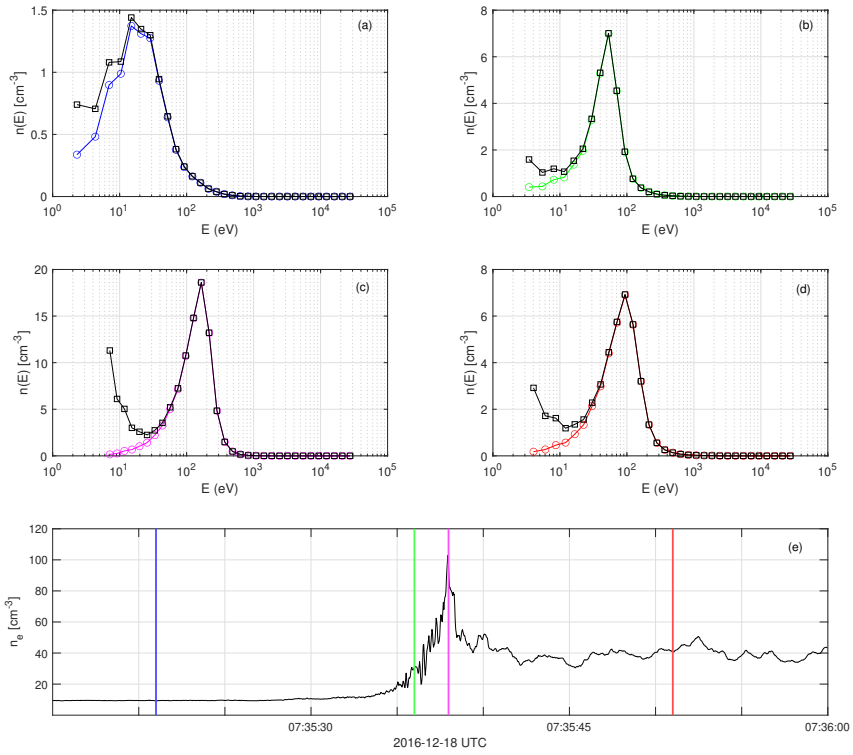

Figure B1. Partial densities at four different locations crossing the shock. In panel (a)-(d) the black curves (and black squares) are calculated using the measured distribution function at MMS1. The colored curves are the same but corrected for secondary electron contamination. Panel (e) shows the measured electron density of MMS1. The colored vertical lines indicate the location of the distribution cuts.

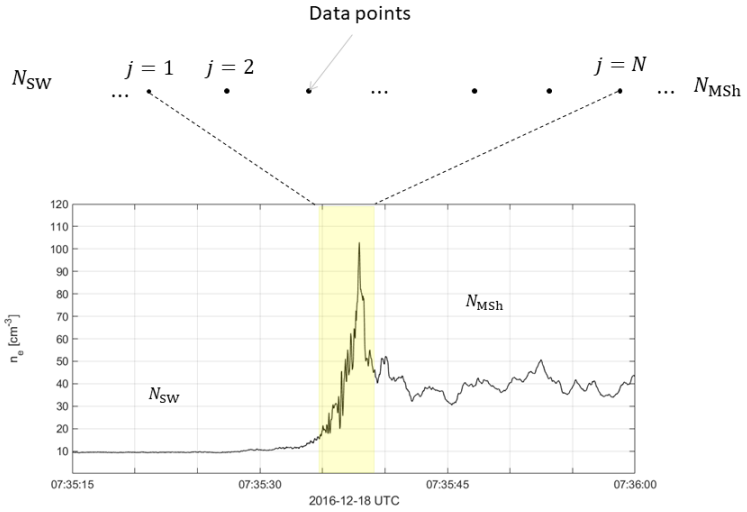

Figure B2. The secondary electron density at the shock is modelled as a gradual transition (shaded yellow area) between the solar wind (N_{SW}) and magnetosheath (N_{MSh}) models using the expression in (B3).

Crossing	SW-model	MSh-model	a	b	η
1	n_{01}	n_{12}	1.0	1.05	1.10
2	n_{01}	n_1	1.0	0.90	1.13
3	n_{01}	n_1	1.0	0.90	1.35
4	n_0	n_2	1.0	1.10	1.31
5	n_1	n_2	1.0	1.00	1.19
6	n_1	n_2	1.0	0.925	1.39
7	n_{01}	n_1	1.0	0.90	1.40
8	n_{01}	n_2	1.0	0.95	1.29
9	n_1	n_2	0.9	1.05	1.38
10	n_{01}	n_1	1.0	0.95	1.04
11	n_{01}	n_1	1.0	1.10	1.24
12	n_1	n_2	1.0	1.10	1.60
13	n_{01}	n_1	1.0	1.25	1.05
14	n_1	n_{12}	1.0	1.00	1.20
15	n_1	n_1	1.0	1.20	1.37
16	n_{01}	n_{12}	1.0	1.00	1.28
17	n_{01}	n_1	1.0	0.75	1.60
18	n_{01}	n_1	1.0	0.75	0.91
19	n_{01}	n_1	1.0	0.90	0.92
20	n_{01}	n_{12}	1.0	1.00	1.05
21	n_{01}	n_1	1.0	1.00	1.10
22	n_{01}	n_1	1.0	1.00	1.44

Table B1. Table showing the secondary electron density models and coefficients used for the 22 shock crossings.

References

Amano, T., Katou, T., Kitamura, N., Oka, M., Matsumoto, Y., Hoshino, M., ... Blake, J. B. (2020, February). Observational Evidence for Stochastic Shock Drift Acceleration of Electrons at the Earth's Bow Shock. *Physical Review Letters*, *124*(6), 065101. doi: 10.1103/PhysRevLett.124.065101

Anderson, J. D. (2004). *Modern compressible flow: With historical perspective.* Boston: McGraw-Hill.

Balogh, A., & Treumann, R. A. (2013). Basic Equations and Models. In A. Balogh & R. A. Treumann (Eds.), *Physics of Collisionless Shocks: Space Plasma Shock Waves* (pp. 45–123). New York, NY: Springer New York. doi: 10.1007/978-1-4614-6099-2_3

Blundell, S. J., & Blundell, K. M. (2010). *Concepts in Thermal Physics.* Oxford University Press.

Cassak, P. A. (2016). Inside the Black Box: Magnetic Reconnection and the Magnetospheric Multiscale Mission. *Space Weather*, *14*(3), 186–197. doi: 10.1002/2015SW001313

Chen, L.-J., Wang, S., Wilson, L. B., Schwartz, S., Bessho, N., Moore, T., ... Avanov, L. (2018, May). Electron Bulk Acceleration and Thermalization at Earth's Quasiperpendicular Bow Shock. *Physical Review Letters*, *120*(22), 225101. doi: 10.1103/PhysRevLett.120.225101

Gershman, D. J., Avanov, L. A., Boardsen, S. A., Dorelli, J. C., Gliese, U., Barrie, A. C., ... Pollock, C. J. (2017). Spacecraft and Instrument Photoelectrons Measured by the Dual Electron Spectrometers on MMS. *Journal of Geophysical Research: Space Physics*, *122*(11), 11,548–11,558. doi: 10.1002/2017JA024518

Howes, G. G. (2018, May). Laboratory space physics: Investigating the physics of space plasmas in the laboratory. *Physics of Plasmas*, *25*(5), 055501. doi: 10.1063/1.5025421

King, J. H., & Papitashvili, N. E. (2005, February). Solar wind spatial scales in and comparisons of hourly Wind and ACE plasma and magnetic field data. *Journal of Geophysical Research: Space Physics*, *110*(A2).

Kivelson, M. G., & Russel, C. T. (1995). *Introduction to Space Physics.* Cambridge University Press.

Krasnoselskikh, V. V., Lembège, B., Savoini, P., & Lobzin, V. V. (2002, April). Nonstationarity of strong collisionless quasiperpendicular shocks: Theory and full particle numerical simulations. *Physics of Plasmas*, *9*(4), 1192–1209. doi: 10.1063/1.1457465

Lalti, A., Khotyaintsev, Y., Graham, D. B., Vaivads, A., Steinvall, K., & Russell, C. T. (2020, December). Source of Whistler Precursor Waves At Quasi-Perpendicular Super-Critical Shocks. *arXiv:2011.10593 [physics]*.

Liang, H., Barbhuiya, M. H., Cassak, P. A., Pezzi, O., Servidio, S., Valentini, F., & Zank, G. P. (2020, October). Kinetic entropy-based measures of distribution function non-Maxwellianity: Theory and simulations. *Journal of Plasma Physics*, *86*(5). doi: 10.1017/S0022377820001270

Liang, H., Cassak, P. A., Servidio, S., Shay, M. A., Drake, J. F., Swisdak, M., ... Delzanno, G. L. (2019, August). Decomposition of Plasma Kinetic Entropy into Position and Velocity Space and the Use of Kinetic Entropy in Particle-in-Cell Simulations. *Physics of Plasmas*, *26*(8), 082903. doi: 10.1063/1.5098888

Oka, M., III, L. B. W., Phan, T. D., Hull, A. J., Amano, T., Hoshino, M., ... Lindqvist, P. A. (2017, June). Electron Scattering by High-frequency Whistler Waves at Earth's Bow Shock. *The Astrophysical Journal*, *842*(2), L11. doi: 10.3847/2041-8213/aa7759

Parks, G. K., Lee, E., McCarthy, M., Goldstein, M., Fu, S. Y., Cao, J. B., ... Fazakerley, A. (2012, February). Entropy Generation across Earth's Collisionless Bow Shock. *Physical Review Letters*, *108*(6), 061102. doi: 10.1103/PhysRevLett.108.061102

Paschmann, G., & Daly, P. W. (1998). Analysis Methods for Multi-Spacecraft Data. , 536.

Pollock, C., Moore, T., Jacques, A., Burch, J., Gliese, U., Saito, Y., ... Zeuch, M. (2016, March). Fast Plasma Investigation for Magnetospheric Multiscale. *Space Science Reviews*, *199*(1), 331–406. doi: 10.1007/s11214-016-0245-4

Raptis, S., Karlsson, T., Plaschke, F., Kullen, A., & Lindqvist, P.-A. (2020). Classifying Magnetosheath Jets Using MMS: Statistical Properties. *Journal of Geophysical Research: Space Physics*, *125*(11), e2019JA027754. doi: 10.1029/2019JA027754

Schwartz, S. J., Henley, E., Mitchell, J., & Krasnoselskikh, V. (2011, November).

414 Electron Temperature Gradient Scale at Collisionless Shocks. *Physical Review*
415 *Letters*, *107*(21), 215002. doi: 10.1103/PhysRevLett.107.215002
416 See, V., Cameron, R. F., & Schwartz, S. J. (2013, April). Non-adiabatic electron be-
417 haviour due to short-scale electric field structures at collisionless shock waves.
418 *Annales Geophysicae*, *31*, 639–646. doi: 10.5194/angeo-31-639-2013